*J. Fluid Mech.* (2025), *vol*. 1002, A51, doi:10.1017/jfm.2024.1197

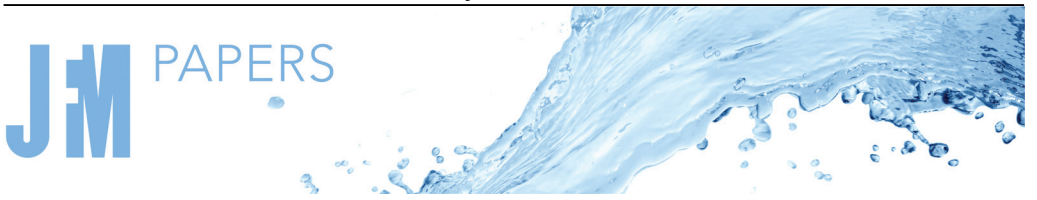

# Turbulent shear flow without vortex shedding, Reynolds shear stress and small-scale intermittency

**K. Steiros[1],†, M. Obligado[2], P. Bragança[2], C. Cuvier[2] and J.C. Vassilicos[2]**

[1]Department of Aeronautics, Imperial College London, London SW7 2AZ, UK

[2]Université de Lille, CNRS, ONERA, Arts et Metiers Institute of Technology, Centrale Lille, UMR 9014-LMFL-Laboratoire de Mécanique des Fluides de Lille – Kampé de Fériet, F-59000 Lille, France

(Received 9 January 2024; revised 14 September 2024; accepted 26 November 2024)

This work presents an experimental investigation of the effects of vortex shedding suppression on the properties and recovery of turbulent wakes. Four plates, properly modified so that they produce different vortex shedding strengths, are tested using high speed particle image velocimetry and hot-wire anemometry, and analysed using spectral proper orthogonal decomposition, mean-flow linear stability analysis and various turbulence statistics. When present, vortex shedding is found to exhibit a characteristic frequency that scales with the mean shear, providing a link between the mean flow and the main turbulent motion. To achieve full suppression of shedding, we combine the effects of porosity and fractal perimeter. The mean shear is then decreased to the point where the flow becomes convectively unstable and shedding vanishes. In that case, the onset of self-similarity is delayed, compared with the case with vortex shedding, and appears after another large-scale structure, the secondary vortex street, emerges. It is also found that both large- and small-scale intermittency are starkly reduced when shedding is absent. A simple theoretical representation of the wake dynamics explains the evolution of the wake properties and its connection to the coherent structures in the flow.

**Key words:** vortex streets, intermittency

## 1. Introduction

Understanding and modelling the physics of the turbulent wake is of primary importance to various applications of the transportation and energy sectors, where bluff body

† Email address for correspondence: k.steiros@imperial.ac.uk

© The Author(s), 2025. Published by Cambridge University Press. This is an Open Access article, distributed under the terms of the Creative Commons Attribution licence (http://creativecommons.org/licenses/by/4.0), which permits unrestricted re-use, distribution and reproduction, provided the original article is properly cited.



https://doi.org/10.1017/jfm.2024.1197 Published online by Cambridge University Press

aerodynamics play a central role. When analysing its dynamics, the turbulent wake is conventionally divided into a near non-self-preserving region and a subsequent self-preserving region (Tennekes & Lumley 1972; Bempedelis & Steiros 2022), the region of self-preservation starting several bluff body characteristic lengths downstream of the bluff body (Bevilaqua & Lykoudis 1978; Nedić, Vassilicos & Ganapathisubramani 2013*b*; Dairay, Obligado & Vassilicos 2015; Obligado, Dairay & Vassilicos 2016). When self-preservation occurs, it allows for a significant simplification of the flow dynamics by reducing the number of the flow variables that govern the flow evolution subject to constraints via the Reynolds-averaged budget equations (Tennekes & Lumley 1972; Townsend 1976).

It is therefore critical to understand when and under which conditions a wake becomes self-preserving. It has been postulated (Townsend 1956, 1970, 1976) that self-preservation is the result of a loss of memory of inlet/initial conditions, i.e. when the flow has departed sufficiently from the bluff body, so that its details are forgotten. However, Bevilaqua & Lykoudis (1978) experimentally demonstrated that self-preservation can coexist with turbulence memory carried by large coherent structures that form close to the body. This led to the hypothesis that self-preservation of the mean velocity and Reynolds stress profiles appears when large scale coherent structures can provide the necessary connection between turbulent fluctuations and the mean flow.

Several types of large-scale coherent structures may exist in a turbulent wake, generated by different instabilities (see e.g. Williamson 1996; Prasad & Williamson 1997; Castro 2005). Bevilaqua & Lykoudis (1978) focused on the large-scale vortices that are shed from the bluff body, i.e. vortex shedding. This is perhaps the most widely studied instability of the turbulent wake because it induces large velocity and pressure fluctuations which, on one hand, significantly influence the average flow field (Mantič-Lugo, Arratia & Gallaire 2014) and, on the other, generate periodic loads on the bluff body (Williamson & Govardhan 2004). Even though vortex shedding has been studied for more than a century, a universal explanation for its emergence has not been put forward. Still, several passive ways for controlling the amplitude of vortex shedding have been proposed. Gerrard (1966) postulated that a growing vortex is shed the moment it is large enough to draw opposite-signed vorticity from the other shear layer across the wake. Indeed, the shedding of vortices can be suppressed by impeding the interaction of the two shear layers, e.g. with the introduction of a splitter plate in the wake (Anderson & Szewczyk 1997; Steiros & Hultmark 2018). If shear layers are allowed to interact, vortex shedding will occur, but can still be attenuated by reducing the mean velocity gradient in the wake, e.g. by introducing fluid bleeding in the bluff body 'base' (Castro 1971; Steiros *et al.* 2020). Shedding attenuation can also be achieved by introducing irregularities on the perimeter of the bluff body (Law & Jaiman 2018). In the case of flat plates, irregularities that follow a multiscale/fractal pattern have been shown to be particularly effective for vortex shedding suppression (Nedić, Ganapathisubramani & Vassilicos 2013*a*; Steiros *et al.* 2017). It should be noted that no matter the suppression technique, a simple inspection of the flow field is not sufficient to determine whether vortex shedding has been completely eliminated, as sharp frequencies in the velocity signal of the near wake may persist even when coherent vortices cannot be easily discerned (Castro 1971). It is thus important to properly extract and assess the flow structures that correspond to these spectral peaks, e.g. via the use of modal decomposition techniques (Lumley 1970; Towne, Schmidt & Colonius 2018).

Bevilaqua & Lykoudis (1978) also studied a turbulent wake where vortex shedding was completely suppressed via the use of high base bleeding. In that case, it was found that the onset of self-preservation was significantly delayed, compared with a wake that allowed for



https://doi.org/10.1017/jfm.2024.1197 Published online by Cambridge University Press

the formation of vortex shedding. To be consistent with their hypothesis of a connection between coherent structures and self-preservation (see above) Bevilaqua & Lykoudis (1978) postulated that, instead of vortex shedding eddies, this type of self-preservation was connected to the emergence of 'vortex-pair' eddies. The existence of these hypothetical structures was based on the earlier works of Grant (1958) and Townsend (1976), who inferred these vortices from measurements of the velocity correlation function in the very far wake (of the order of 500 body diameters). The vortex-pair vortices were hypothesised to form due to the straining of turbulence by the mean flow, i.e. without the influence of the bluff body's initial conditions, as per the Townsend self-preserving hypothesis. Still, Bevilaqua & Lykoudis (1978) did not attempt to identify the formation of such vortices in the self-preserving part of the flow.

It is noteworthy to mention that the subsequent smoke visualisation experiments of Cimbala, Nagib & Roshko (1988) hinted that such vortex-pair eddies may originate from earlier vortical structures which appear between $O(10)$ and $O(100)$ diameters downstream of the body, and are known as the 'secondary vortex street' (in contrast to the 'primary' Kármán street closer to the body). Numerous studies have investigated these secondary vortices in both laminar and turbulent regimes, see for instance Wygnanski, Champagne & Marasli (1986); Cimbala *et al.* (1988); Williamson & Prasad (1993); Huang, Kawall & Keffer (1996); Huang & Keffer (1996) and Jiang & Cheng (2019). Their formation has been attributed to both the strain of turbulence by the mean flow (Cimbala *et al.* 1988), and the interaction and merging of earlier vortices that form in the vicinity of the body (Huang & Keffer 1996). The exact formation mechanism of these secondary vortices is not the focus of the current work, but we note its potential relevance to the Townsend self-preserving hypothesis.

We close this brief review by noting that, if the hypothesis of Bevilaqua & Lykoudis (1978) is accurate, i.e. if self-preservation is a manifestation of the coupling between the mean flow and the 'main turbulent motion' (to use Townsend's terminology) via large-scale coherent structures, then this could mean that various self-preserving behaviours exist for the same flow type (e.g. wake), depending on the dominant structure at play. Indeed, Bevilaqua & Lykoudis (1978) found that self-preservation connected with vortex shedding produced characteristic length and velocity scales with starkly different growth rates, compared with self-preservation when vortex shedding is absent. No mention of small-scale differences was made in their work. However, it is now known, since the works of Nedić *et al.* (2013*b*), Dairay *et al.* (2015), Obligado *et al.* (2016), Cafiero & Vassilicos (2019), Chongsiripinyo & Sarkar (2020) and Ortiz-Tarin, Nidhan & Sarkar (2021), that different small-scale turbulence dissipation scalings lead to different growth rates of the mean-flow velocity and length scales during self-similar evolution. It is therefore not inconceivable that differences in large-scale coherent structures such as those discussed by Bevilaqua & Lykoudis (1978) may also lead to differences in the small scales of the turbulence and the cascade as a whole (see Goto & Vassilicos 2016; Alves Portela, Papadakis & Vassilicos 2018). In particular, while vortex shedding was found by Bevilaqua & Lykoudis (1978) to generate large-scale intermittency at the edges of the wake due to the rapid alternation between slow fluctuations of low intensity and rapid fluctuations of high intensity, small-scale intermittency was not examined by them and the works of the past ten years mentioned above make it conceivable that coherent structures may also have a direct effect on small-scale intermittency. Demonstrating such an effect is one of this paper's aims.

Based on the above discussion, the primary goal of this work is to shed some light on two issues. First, is the hypothesis of Bevilaqua & Lykoudis (1978) justified,



https://doi.org/10.1017/jfm.2024.1197 Published online by Cambridge University Press

i.e. does self-preservation come hand-in-hand with the emergence of large-scale vortices in the turbulent wake? More specifically, if vortex shedding were to be suppressed, would self-preservation disappear and reappear only when another large-scale coherent structure is formed? Our findings hint that this is indeed the case. Second, are small scales sensitive to the different types of large structures, i.e. do different types of self-preservation alter the cascade as a whole?

To answer these questions, this paper reports on four bluff body wakes whose level of vortex shedding was carefully varied by combining two shedding suppression methods: base bleeding and multiscale perimeter modification. We note that these choices do not exhaust the possibilities for wake suppression. The potential to suppress shedding is characterised via modal decomposition and linear stability analysis techniques. The extracted characteristic frequencies are found to scale with mean-flow properties, in support of the ideas of Roshko (1955). Our results confirm and strengthen the finding of Bevilaqua & Lykoudis (1978) that, with decreasing vortex shedding, the wake becomes self-preserving further downstream from the bluff body. We find that, when vortex shedding is completely suppressed, self-preservation occurs when other large-scale structures, namely the secondary vortices, emerge. Furthermore, we find that small-scale intermittency is dependent on the type of coherent structure present, and in fact increases with vortex shedding intensity. Finally, with regard to the connection between turbulence and mean flow that Bevilaqua & Lykoudis (1978) considered necessary for self-preservation, we advance a mechanism based on the vortex shedding's generation of Reynolds shear stresses.

The structure of the article is as follows. Section 2 presents the experimental procedure and post-processing methodology employed in the study. Section 3 characterises the vortex shedding properties and describes its influence on the near and far turbulent wake. Finally, § 4 draws the conclusions of this study.

## 2. Methodology

### 2.1. *Experimental details*

Experiments were conducted in the Lille wind tunnel at Lille Fluid Mechanics Laboratory (LFML). The tunnel test section is 1 m × 2 m × 21 m and is temperature regulated. The free-stream velocity was set to $U_\infty = 7.5\ \mathrm{ms}^{-1}$. At that speed, the turbulence intensity is 0.2 % when the tunnel is empty. Four types of plate shapes were tested (see figure 1): a solid circular plate (C), a circular plate of 40 % porosity (PC), a solid fractal plate (F) and a fractal plate of 40 % porosity (PF). Both fractal plates had two fractal iterations and were designed via the procedure described in Nedić *et al.* (2013*a*). All plates were 3D printed. The circular plate diameter was $D = 105$ mm, and the gross area (i.e. before perforating PC and PF) of all plates was identical. The plate thickness was 4 mm. The global Reynolds number was $Re = DU_\infty/\nu = 52\,500$, where $\nu$ is the kinematic viscosity of air corresponding to a fully turbulent regime. The plates were suspended in the middle of the cross-section via the use of four piano strings, attached to a small bracket bolted on the centre of the plates. Visual inspection showed that the plate vibrations were negligible.

Hot-wire anemometry (HWA) measurements were conducted using a single Pt-W 5 micron wire, 3 mm long, with a 1.25 mm sensing element. The probe was driven by a TSI IFA300 anemometer. The acquisition frequency was set to 50 kHz with a low-pass filter at 20 kHz. For each measurement point, the acquisition time was 180 s. Calibrations of the probe were conducted at the beginning and end of each measurement campaign. It was verified that for all datasets we had at least $k_w\eta = 1$, where $k_w = 2\pi f/U$. In the above,



https://doi.org/10.1017/jfm.2024.1197 Published online by Cambridge University Press

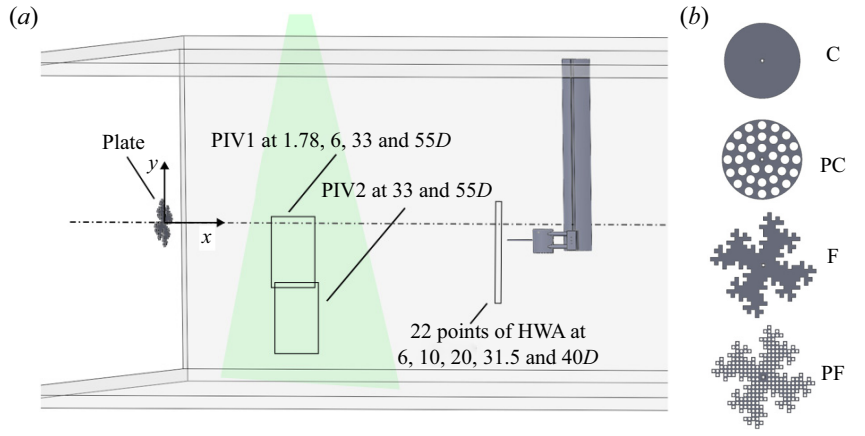


Figure 1. (*a*) Experimental configuration showing the plate mounting location and PIV/HWA measurement plane dimensions. The PIV and HWA experiments were conducted at multiple downstream locations, as indicated in the figure. (*b*) The various plates tested. From top to bottom: solid circular plate – C, porous circular plate – PC, solid fractal plate – F and porous fractal plate – PF. The characteristic diameter is $D = 105$ mm.

$\eta$ is the Kolmogorov scale, $f$ the Fourier frequency and $U$ the local time-averaged velocity. The probe was translated using a vertical traverse system (see figure 1*a*), to conduct measurements at 22 equidistant points, located at $0.76 > y/D > -2.1$ with respect to the centreline. Measurements were conducted at five locations downstream of the plate ($6D$, $10D$, $20D$, $31.5D$ and $40D$) by manually moving the traverse system.

High-speed planar particle image velocimetry (PIV) measurements were conducted using a Quantronix high-speed laser and a 4MP Miro camera equipped with a 200 mm objective lens with an f-number equal to 5.6. The acquisition frequency was set to 100 Hz. The time separation between frames was between 90 and 180 ms, depending on the field of view. The seeding was water and glycol droplets of approximately 1 µm. To obtain the vector fields, multipass processing was performed, with a final pass at $24 \times 24$ windows and 60 % overlap, leading to a final interrogation window size of 1.8 mm. Measurements were conducted in vertical streamwise (streamwise $x$, lateral $y$) planes of size $1.1D \times 1.78D$ (see figure 1*a*) which could be moved at various locations by translating the laser sheet and camera. For each case, 15 runs of 1018 velocity fields were acquired, resulting in 15 270 fields. The wakes of the plates C, F and PF were measured in the top plane $0.17 > y/D > -1.61$ (see PIV1 plane in figure 1*a*), at distances $1.78D$, $6D$, $33D$ and $55D$ downstream of the plate. At distances $33D$ and $55D$, measurements were also conducted in the bottom plane $-1.40 > y/D > -3.20$ (see PIV2 plane in figure 1*a*) for the C, F and PF plates, in order to capture the full wake which, due to its expansion, exceeded the boundaries of the PIV1 window. For those locations, the two measured planes were stitched together. Additionally, the wakes of the PC plate were measured on the top plane $0.17 > y/D > -1.61$, at downstream distances $1.78D$ and $6D$. The measurement locations for the PIV and HWA experiments are summarised in table 1. Figure 2 shows example PIV snapshots at the near field of view of the four tested plates.

### 2.2. *Post-processing methodologies*

#### 2.2.1. *Spectral proper orthogonal decomposition*

Spectral proper orthogonal decomposition (SPOD) was used to characterise the vortex shedding structures emanating from the different plates. The simpler approach of binning



https://doi.org/10.1017/jfm.2024.1197 Published online by Cambridge University Press

| | PIV | | | HWA |
|---|---|---|---|---|
| $y$-location | Top (PIV1) | Top (PIV1) | Bottom (PIV2) | $0.76 > y/D > -2.1$ |
| $x$-location | 1.78, $6D$ | 33, $55D$ | 33, $55D$ | 6, 10, 20, 31.5, $40D$ |
| Plates | C, PC, F, PF | C, F, PF | C, F, PF | C, PC, F, PF |

Table 1. Measurement locations for each plate, for the PIV and HWA conducted in this study.

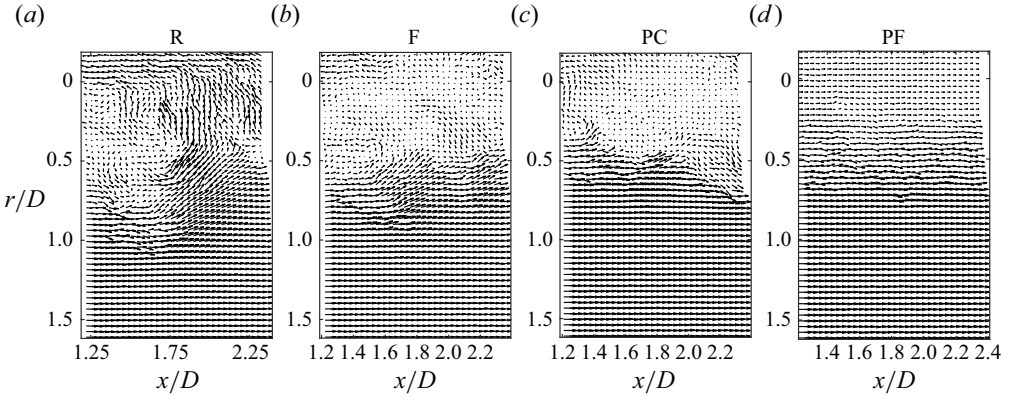


Figure 2. Example velocity snapshots for the four plates tested in the near PIV field.

the high-speed PIV measurements to produce phase averages was first attempted, but produced results which greatly resembled the total time average of the flow, instead of the various phases of the coherent structure. This was thought to occur due to two reasons. First, because the acquisition frequency of the PIV system could not be set to an exact integer multiple of the average shedding frequency. Second, because turbulent vortex shedding is not a strictly periodic phenomenon, but is rather characterised by a broad range of frequencies.

A partial solution to the above is SPOD, which solves the eigenvalue problem of the Fourier transform of the two-point space–time correlation tensor (Sieber, Paschereit & Oberleithner 2016; Towne *et al.* 2018). In that way, modes that optimally represent the second-order space–time flow statistics and oscillate at specific frequencies (i.e. have time coherence) can be obtained. It can then be argued that the most energetic modes which correspond to frequencies close to the ones of vortex shedding will be representative of that phenomenon. The SPOD approach does not solve the issue that vortex shedding is only quasi-periodic, and therefore its dynamics is distributed into multiple frequencies, but ensures that the produced frequency-locked modes will contain information from the most relevant frequency, and not from frequencies which are unrelated to the coherent structure.

To obtain the SPOD modes from our PIV data, the algorithm described in Towne *et al.* (2018) is used, where the PIV snapshots are separated in an ensemble of $N$ realisations, with each realisation containing the evolution of a quantity (in our case the radial velocity fluctuations $u_r$) in axial and radial coordinates, respectively, $x$, $r$, and time $t$. Note that we consider a polar coordinate transformation, which for our planar data means that the axial coordinate $x$ is the same as the streamwise $x$ considered before, while the radial coordinate $r$ is effectively the same as the vertical coordinate $y$. Subsequently, discrete



https://doi.org/10.1017/jfm.2024.1197 Published online by Cambridge University Press

Fourier transform is applied to the ensemble which consists of $N$ realisations of the evolution of the scalar in space $x$, $r$ at different frequencies $f$. This allows the formulation of an $N \times N$ spectral eigenvalue problem for the 'cross-spectral density tensor' (i.e. the Fourier transform of the space–time correlation tensor evaluated at a particular frequency), which is repeated for each of the desired frequencies. For each frequency a set of spatial eigenmodes is produced, ranked according to the magnitude of their eigenvalues. For our experiments, only the first (most energetic) mode exhibited distinctive peaks at the shedding frequency. For more information on the SPOD algorithm see Towne *et al.* (2018).

### 2.2.2. *Local linear stability analysis of the average flow*

While the SPOD analysis is a great tool in extracting periodic instabilities from the flow field, it cannot reveal whether they are absolute or convective in nature (see later in the section for these definitions). To further examine the nature of the periodic instabilities in the vicinity of the four plates, we performed stability analysis on the time-averaged axial flow profiles, which are not stationary solutions of the Navier–Stokes equations. We consider the standard Reynolds decomposition $\hat{u}_j = U_j + u_j$, where $\hat{u}$ is the instantaneous velocity, $U$ the time-averaged velocity and $u$ the instantaneous difference (fluctuation) between the two. The subscript $j$ can be $x$, $r$ or $\theta$, denoting the axial, radial and azimuthal components of velocity, respectively. The average azimuthal velocity, $U_\theta$ is assumed to be zero for all cases, while the wake is assumed locally parallel, i.e. $U_r \approx 0$. Following several authors (Malkus 1956; Triantafyllou, Kupfer & Bers 1987; Cimbala *et al.* 1988; Mantič-Lugo *et al.* 2014; Gupta & Wan 2019; Gupta *et al.* 2020), we consider a 'mean-flow disturbance' which in our case leads to perturbation equations expressed in $(x, r, \theta)$. The perturbations are assumed to be of the form $(\tilde{u}_x, i\tilde{u}_r, \tilde{u}_\theta)\exp(\mathrm{i}(m\theta + kx - \omega t))$, where $\tilde{u}_x$, $\tilde{u}_r$, $\tilde{u}_\theta$ and $\tilde{p}$ are perturbations to the $x, r, \theta$ mean velocities and mean pressure, respectively. In the above, $m$ is the azimuthal wavenumber, $k = k_R + \mathrm{i}k_I$ is the streamwise wavenumber and $\omega = \omega_R + \mathrm{i}\omega_I$ is the angular frequency of the oscillation. The subscripts $R$ and $I$ in $k$ and $\omega$ denote the real and imaginary part of the quantities, respectively. Upon linearisation, the perturbation equations become (see also Gupta & Wan 2019)

$$\left.\begin{aligned} 0 = k\tilde{u}_x + \frac{1}{r}\frac{\partial}{\partial r}(r\tilde{u}_r) + \frac{m}{r}\tilde{u}_\theta, \quad \omega\tilde{u}_x = k\tilde{p} + kU_x\tilde{u}_x + m\frac{\partial U_x}{\partial r}\tilde{u}_r, \\ \omega\tilde{u}_r = \frac{\partial\tilde{p}}{\partial r} + kU_x\tilde{u}_r, \quad \omega\tilde{u}_\theta = \frac{m}{r}\tilde{p} + kU_x\tilde{u}_\theta. \end{aligned}\right\} \tag{2.1}$$

Stability analysis is performed based on the Chebyshev spectral collocation method, with the discretisation in the radial direction performed on a Gauss–Lobatto–Chebyshev grid. This is mapped on a radially unbounded space $r/D = \zeta/(1 - \zeta^2 + 1/R_{max})$, where $\zeta$ is the Chebyshev grid from 0 to 1 and $R_{max} = 25$ is large enough to represent an unbounded space. The number of collocation points used was $N = 120$. Increasing both $R_{max}$ and $N$ did not alter appreciably the results. More information on the numerical method can be found in Gupta & Wan (2019).

The above analysis was used to determine whether an observed instability is of the absolute or convective type. If an impulsive disturbance grows exponentially at the location of its generation (i.e. its group velocity $\partial\omega/\partial k$ is zero) the flow is termed absolutely unstable (Kupfer, Bers & Ram 1987; Gupta & Wan 2019). If, on the other hand, the produced wave packet is convected downstream (group velocity non-zero), leaving the flow at the location of its generation undisturbed, the instability is of the convective type. The Kármán vortex street is generally accepted to originate from an absolute instability



https://doi.org/10.1017/jfm.2024.1197 Published online by Cambridge University Press

region close to the bluff body, shifting to a convective instability further downstream (Triantafyllou *et al.* 1987; Williamson 1996).

To determine whether the near wake of the four tested plates is subjected to an absolute instability (vortex shedding) the 'cusp' method is used (Kupfer *et al.* 1987; Hwang & Choi 2006). The spatio-temporal problem is solved, where the system of the above equations receives the input of a complex wavenumber, and yields a complex frequency as output. This procedure is repeated for a grid of complex $k$ values, which are mapped on isolines of $k_I = \text{const}$ at the complex omega plane. The absolute frequency $\omega_0$ is then identified at the end of a typical cusp-like trajectory. If a cusp point is characterised by a positive imaginary part, the instability is of the absolute type, whereas if no cusp with positive imaginary part exists, only convective (amplifier) instabilities exist in the flow field. In our case, it was made sure that the requirement of the cusp point being covered only once by the image of $k_I = 0$ on the omega plane was fulfilled.

The above analysis has two significant limitations. First, it assumes that the average flow is locally parallel (i.e. that the average radial velocity is negligible). While this assumption can be thought correct in the far, self-preserving wake (Tennekes & Lumley 1972; Cimbala *et al.* 1988), it is questionable in the near wake where the Kármán street originates. Still, previous studies have indicated that local weakly non-parallel stability analysis at the near wake of bluff bodies yields accurate predictions regarding the onset of vortex shedding and the frequencies involved (see e.g. Triantafyllou *et al.* 1987). The second limitation is that the above analysis assumes that the mean-flow disturbance does not alter the Reynolds stresses of the flow (Malkus 1956), i.e. that turbulence remains 'frozen' under perturbations. Again, this assumption is questionable for high Reynolds number flows. However, there is an abundance of works in the literature (see for instance Triantafyllou *et al.* 1987; Cimbala *et al.* 1988; Gupta & Wan 2019) which suggests that the above linearised analysis yields accurate predictions even at very high Reynolds numbers, and in a variety of shear flows.

### 2.2.3. *Zero crossings*

A complementary analysis is also performed using the zero crossings of the streamwise fluctuating velocity $u_x$. This approach allows us not only to characterise various length scales of a turbulent flow (Mazellier & Vassilicos 2008; Mora *et al.* 2019; Ferran, Aliseda & Obligado 2023) but also its intermittency (Mazellier & Vassilicos 2008). The Rice theorem, when adapted to turbulent flows (Liepmann & Robinson 1953) allows us to estimate the Taylor micro-scale $\lambda$. In particular, it can be mathematically proved that $\lambda$ is proportional to the average distance $\bar{l}$ between zero-crossing points: $\bar{l} = B\lambda$. The constant $B$ is defined as $B = C_1\pi$, where $C_1$ is a constant that quantifies the non-Gaussianity of velocity derivatives $(\mathrm{d}u_x/\mathrm{d}x)$. For a Gaussian distribution $C_1 = 1$, and $C_1 > 1$ for an intermittent small-scale turbulence. More specifically, the analytical expression of this constant is (Mazellier & Vassilicos 2008)

$$C_1 = \sqrt{\frac{2}{\pi}}\frac{\sqrt{\overline{\left(\dfrac{\mathrm{d}u_x}{\mathrm{d}x}\right)^2}}}{\overline{\left|\dfrac{\mathrm{d}u_x}{\mathrm{d}x}\right|}}, \tag{2.2}$$

with the overline denoting the time average. The constant $C_1$ provides a simple way to quantify small-scale intermittency via the non-Gaussianity of the streamwise derivative of $u_x$. A larger value of $C_1$ therefore implies a more intermittent small-scale turbulence.



https://doi.org/10.1017/jfm.2024.1197 Published online by Cambridge University Press

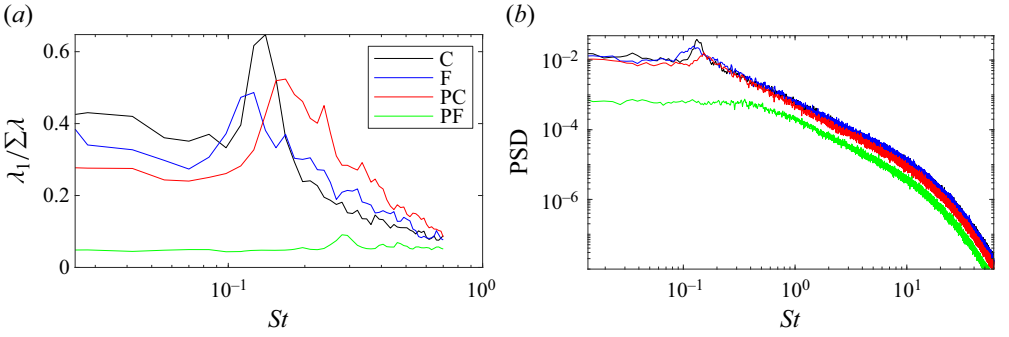


Figure 3. (*a*) Eigenvalue of the first SPOD mode, normalised with the sum of the eigenvalues for all modes, evaluated at each $St$ for the four tested plates. Results are shown for the cross-wise velocity component at the near-wake PIV window ($x/D \approx 1.78$). (*b*) The HWA spectra $10D$ downstream, $1D$ below the centreline.

## 3. Results and discussion

### 3.1. *Characterisation of vortex shedding*

#### 3.1.1. *Vortex shedding attenuation*

We first test the effect of the plate modifications (see figure 1*b*) in the near wake, aiming at a gradual attenuation of vortex shedding intensity. Figures 3 and 4 show the results of the SPOD analysis for the radial velocity component at the near PIV field ($x/D \approx 1.78$). Figure 3 plots the eigenvalue of the first SPOD mode of each plate, over a range of Strouhal numbers $St = fD/U_\infty$, normalised with the total energy at each Strouhal number (i.e. the sum of the eigenvalues of all modes). The plates C, F and PC exhibit peaks at Strouhal numbers of 0.13, 0.12 and 0.16, respectively, indicating the presence of coherent vortices. These values agree with the ones measured with the hot-wire for the streamwise velocity component (see figure 3*b*). As expected, the relative energy of F and PC plates is significantly lowered compared with the one of the C plate, due to the shedding–attenuating effect of wake bleeding and the fractal perimeter, already documented in Castro (1971) and Nedić *et al.* (2013*b*), respectively. Remarkably, the combination of both types of modifications (i.e. PF plate) completely eliminates the peak, producing only a very small bump at $St = 0.29$ (see figure 3*a*), suggesting a further (if not total) elimination of vortex shedding. We note that the 'spectra' of the suboptimal eigenvalues did not exhibit any distinctive peaks (not plotted).

The above conclusions are also supported by the shapes of the first SPOD modes corresponding to the most energetic Strouhal number (i.e. at the peaks of figure 3*a*), plotted in figure 4. It can be seen that the C, F and PC plates exhibit strong alterations of the radial fluctuating velocity, spanning almost the whole PIV window, indicating the presence of a vortex. Even though the modes are qualitatively similar, there is a slight decrease in radial extent of the structure, from the C to the F and then to the PC plate. The characteristic mode of the PF plate is more fragmented, and remains confined to the upper section of the PIV window, suggesting that the $St = 0.29$ peak corresponds to a shear layer, rather than a vortex shedding type of instability. In Appendix A we show that the conclusions of the SPOD analysis are independent of the relative angle of the PIV plane with respect to the fractal plates.

It is noteworthy to mention that Castro (1971) proposed that two-dimensional porous plates completely suppress vortex shedding for plates beyond 20 % porosity, based on the observation of a sudden kink in the measured wake Strouhal number and drag coefficient



https://doi.org/10.1017/jfm.2024.1197 Published online by Cambridge University Press

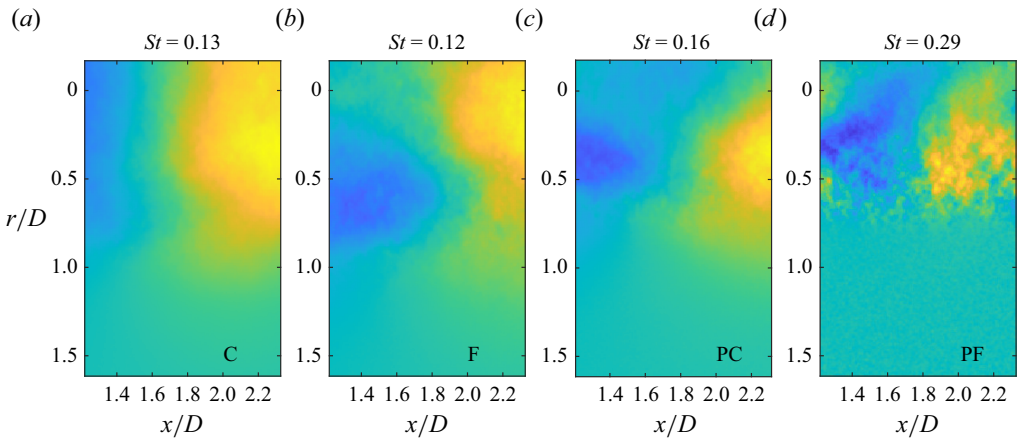


Figure 4. Shape of the first SPOD mode of the radial velocity $u_r$ at the dominant frequency for each case, at the PIV windows closest to the plate. Here, C, circular plate; F, fractal plate; PC, porous circular plate; and PF, porous fractal plate.

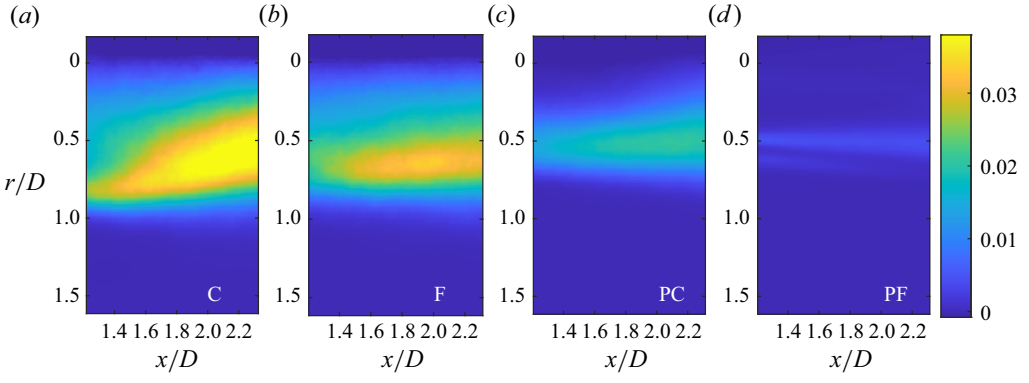


Figure 5. Normalised cross-term of the Reynolds stresses, $\overline{u_x u_r}/U_\infty^2$, for the four tested plates at the near-wake PIV window.

at that value. The peaks in the measured spectra found by Castro at higher porosities were instead attributed to a flapping type of instability of the shear layers. Here, we instead show that the porous circular plate exhibits clear traces of vortex shedding, even at 40 % porosity, contrary to the postulation of Castro. Evidently, there seems to be a sudden change in the nature of vortex shedding at 20 % porosity, generating the kink that Castro (1971) observed, but shedding does not completely disappear. Low-order models (Steiros & Hultmark 2018; Steiros, Bempedelis & Ding 2021) and recent measurements (Cicolin *et al.* 2024) suggest that, at large porosities, vortex shedding is of low intensity, and occurs sufficiently far from the plate, so that it has a negligible effect on the plate drag.

Figure 5 shows the Reynolds shear stress, $\overline{u_x u_r}$, of the different plates (the overline denotes time average). A gradual decrease of stresses can be observed, both in magnitude and extent, as the plate changes from the C to the F, PC and PF plate. The PF case exhibits very small stress values confined to the shear layer (i.e. around $r/D = 0.5$), suggesting a shear-layer instability, in agreement with the SPOD results. Appendix A investigates the variation of the Reynolds shear stresses and mean streamwise velocities of the fractal plates with the relative angle of the PIV field of view, relevant to the plates.



https://doi.org/10.1017/jfm.2024.1197 Published online by Cambridge University Press

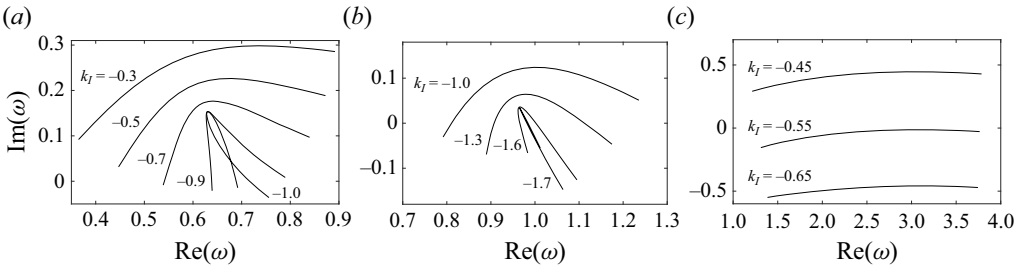


Figure 6. Examples of the cusp method for the (*a*) F, (*b*) PC and (*c*) PF plates at $x/D = 1.4$. The $x$-coordinate of the cusp corresponds to the frequency of the absolute instability (if it corresponds to a positive $y$-coordinate). No cusp is found for the PF plate, suggesting only convective instabilities there.

The results of the SPOD and Reynolds stress analysis suggest that vortex shedding might be completely eliminated in the PF plate case. To investigate this further, we performed local linear stability analysis on the average $U_x$ velocity profiles of the PIV1 window ($U_\theta$ and $U_r$ are assumed negligible), for each plate. Using the cusp method, we found that the $m = \pm 1$ modes of the C, F and PF plates exhibit an absolute instability at Strouhal numbers of 0.1, 0.1 and 0.15, respectively (see some examples in figure 6), not too far from the experimentally determined ones (see the titles of panels in figure 4). The $C$ plate exhibits an absolute instability for all streamwise distances considered (i.e. $1.2 < x/D < 2.3$) while the F and PC plates exhibit an absolute instability only for $x/D < 2$ and $x/D < 1.45$, respectively. No absolute instability could be determined for the PF plate at any azimuthal mode, providing further support of the claim that the PF modification completely eliminates vortex shedding.

### 3.1.2. *Vortex shedding frequency scaling*

The previous section indicates that a local linear stability analysis of the mean flow is relatively successful in reproducing the value of the characteristic frequency of vortex shedding if applied at the very near-wake location, in agreement with previous works (see for instance Triantafyllou *et al.* 1987). This success hints that the shedding frequency at the very near wake (i.e. at the vortex-formation location) is primarily connected to the streamwise velocity gradient of the average flow, i.e. $f = f(\partial U_x/\partial r)$. On dimensional grounds, we may thus define a revised Strouhal number as

$$St^* = \frac{f}{\frac{1}{2}\frac{\partial U_x}{\partial r}}, \tag{3.1}$$

which we might expect to have a constant value for any of the plates tested and to be applicable in the near vicinity of the plates (the coefficient 1/2 is added to render this Strouhal number comparable to the one deduced by Roshko (1955), as will be shown shortly). Figure 7 is a plot of the above Strouhal number for the four plates tested, along with the streamwise distance interrogated at the near-wake PIV window. For each plate, the frequency is the same for all $x/D$ and is equal to the one acquired from the SPOD results of figure 3, while the mean velocity gradient was calculated as a first-order approximation, i.e. $\partial U_x/\partial r \approx (U_{x,max} - U_{x,min})/(r_{max} - r_{min})$, where $U_{x,max}$ and $U_{x,min}$ are the maximum and minimum streamwise velocities at a particular cross-section, corresponding to the radial locations $r_{max}$ and $r_{min}$. Note that, due to the proximity of the plate in the near-wake PIV window, $U_{x,max} > U_\infty$, as the flow is locally accelerated in the shear layers; $r_{max}$ is



https://doi.org/10.1017/jfm.2024.1197 Published online by Cambridge University Press

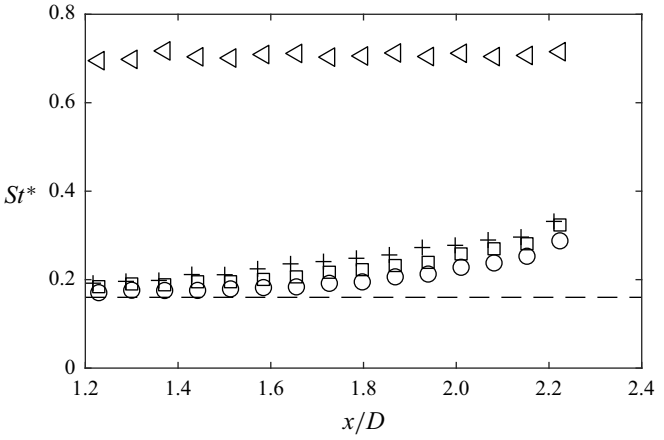


Figure 7. Revised Strouhal number vs normalised downstream distance for the four plates. Circle: C, square: F, cross: PC, triangle: PF. The 'universal' value of Roshko is depicted with a dashed line.

the radial position where this local acceleration is maximum. Here, $r_{min}$ is effectively zero for all plates.

It can be observed that the three plates that exhibit vortex shedding have an almost identical behaviour, while the PF plate is distinctly different, a further indication of its drastically different near-wake physics. The C, F and PC plates exhibit a decreasing $St^*$ as they approach the plate, due to the wake becoming narrower. Even though our PIV window does not allow for an inspection of shorter streamwise distances, the three plates seem to converge to $St^* \approx 0.16$ near the body (where vortex shedding is generated). The vicinity of the body is where (3.1) is expected to hold, and it is noteworthy that there the predicted value approaches the one that Roshko (1955) proposed to be universal for bluff bodies.

The coincidence of our value with Roshko's is not fortuitous as his method for estimating it shares remarkable similarities to ours (despite the obvious differences). Roshko measured a wide range of vortex shedding frequency values, depending on the bluff body and Reynolds number tested, but postulated that the right length and velocity flow scales would collapse them into a single Strouhal value, independent of the body details. To derive those scales, Roshko considered the potential flow model of Kirchhoff (1869) for two-dimensional bluff bodies as a starting point, i.e. as a 'base flow'. Kirchoff's model is known to be inaccurate, but Roshko adjusted it so that its predictions are consistent with the experimentally measured average pressure at the rear side of the various bodies (i.e. base pressure) he tested. Based on that revised Kirchoff model, Roshko then derived predictions for the wake width $d$ and velocity on the dividing streamline $U_s$, which in turn yielded a universal $St \approx 0.16$ for all shedding frequencies, partially confirming his postulation (even though counter-arguments exist, see Gerrard 1966).

Our stability analysis leads to the same conclusion as Roshko's method, and that can be seen from the fact that in his simplified model $\partial U_x/\partial r = 2U_s/d$, i.e. Roshko's Strouhal number definition becomes identical to (3.1). Therefore, both methods identify (via a different starting point) the average velocity gradient as the appropriate normalisation parameter for the vortex shedding frequency. This is in agreement with the idea of Bevilaqua & Lykoudis (1978) that large-scale fluctuations (and the rate that those occur) are intimately connected to the mean flow.



https://doi.org/10.1017/jfm.2024.1197 Published online by Cambridge University Press

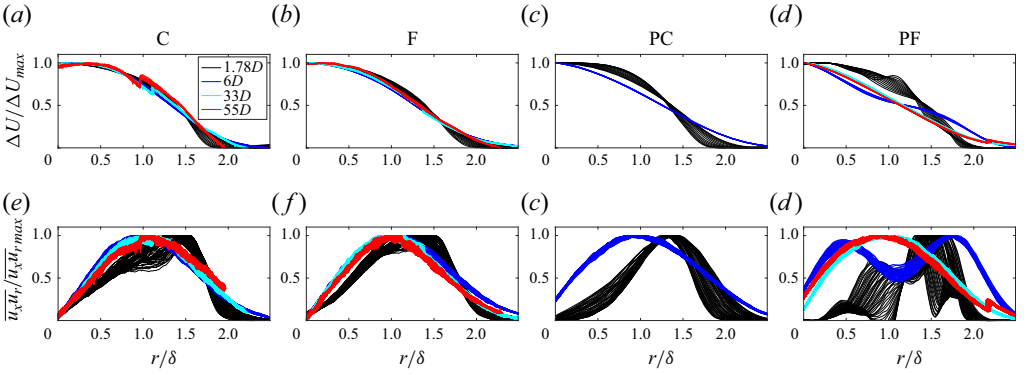


Figure 8. Similarity profiles of streamwise momentum deficit and cross-term of Reynolds stresses, for the four plates. The four colours correspond to the four downstream PIV plane locations, as shown in the top left legend.

## 3.2. *Effect of coherent structures on the wake*

### 3.2.1. *Onset of self-preservation*

Given the variation of the vortex shedding intensity achieved with the various plate modifications, we now proceed to test its effect on the self-preservation of the wake. For that we consider the evolution of the streamwise velocity and the cross-term of the Reynolds stress tensor, shown in figure 8. In particular, we plot the radial distributions of $\Delta U = (U_{x,max} - U_x)$ and $\overline{u_x u_r}$, normalised with their maximum values at each streamwise location (note that $\Delta U_{x,max} = (U_{x,max} - U_{x,min})$), vs the normalised radial coordinate $r/\delta$, with $\delta^2 = (1/\Delta U_{max}) \int_0^\infty \Delta U r \, \mathrm{d}r$. In the near-wake PIV window ($x/D \approx 2$), $U_{x,max}$ is calculated as in § 3.1.2. In the other PIV windows $U_{x,max}$ is effectively $U_\infty$. The upper limit of integration for the calculation of $\delta$ is the lateral end of the PIV domain.

In figure 8 four colours are plotted per panel, corresponding to the four PIV windows considered, i.e. at $x/D = 1.78D$, $6D$, $33D$ and $55D$ (see figure 1), while the multiple lines correspond to different streamwise locations within the PIV windows. The spikes (e.g. see red line at $r/\delta \approx 1$ in panel *a*) correspond to locations where the PIV1 and PIV2 windows were stitched (see figure 1). Note that at long distances downstream the velocity deficit is very small and therefore small errors caused by the stitching lead to large spikes in the normalised velocity deficit. The actual stitching error is actually smaller than $0.5\,\%U_\infty$ (see for instance figure 15*b*). In Appendix B we confront the profiles of the various plates at $55D$ downstream, and show that there is a significant difference in the profile shapes, when vortex shedding is suppressed.

It can be observed that the earliest onset of self-preservation is achieved by the C and F plates, with the streamwise velocity and Reynolds stresses roughly collapsing from the second PIV window ($6D$). The PF plate which lacks the vortex shedding instability exhibits a later onset of self-preservation, only approximately reaching it at the third PIV window, i.e. at $33D$, for both flow quantities. These results confirm and strengthen the earlier conclusion of Bevilaqua & Lykoudis (1978) that vortex shedding accelerates the onset of self-preservation.

A natural question that may arise is whether the delayed onset of self-preservation in the PF case occurs because, in the absence of vortex shedding, another type of large-scale vortical structure needs to be first formed in the wake to render self-similarity possible. As explained in the introduction, this was the hypothesis of Bevilaqua & Lykoudis (1978) that was not, however, verified. Our results indeed suggest that this is the case.



https://doi.org/10.1017/jfm.2024.1197 Published online by Cambridge University Press

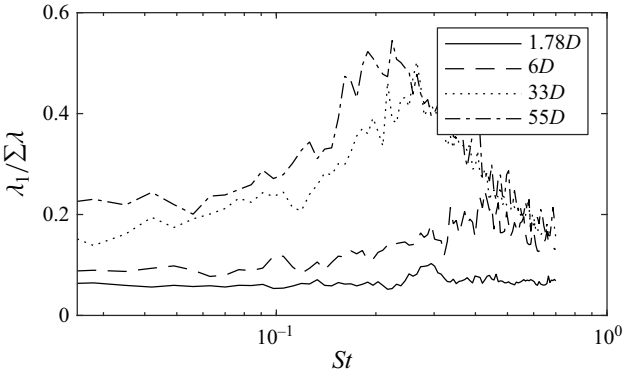


Figure 9. Eigenvalue of the first SPOD mode for the radial velocity component, normalised with the sum of the eigenvalues for all modes, evaluated at each $St$ for the PF plate. Each curve corresponds to a different PIV window downstream of the plate.

Figure 9 plots the normalised eigenvalues of the first SPOD mode for four PIV windows at different downstream distances for the PF case. Well-defined periodicity, reflective of the existence of coherent structures, appears only after $33D$, i.e. at the point where the wake becomes self-preserving. Figure 10 shows the shape of the SPOD modes at the peak Strouhal number of each curve of figure 9, i.e. the most dominant coherent structure at each PIV window. It can be seen that, up until $6D$, the dominant structures are small and confined to the shear layers of the wake, and are thus of the Kelvin–Helmholtz type, while at $33D$ there is indeed the trace of a large-scale structure. By comparing these results with those of Cimbala *et al.* (1988) and Huang & Keffer (1996) for porous strips, it can be deduced that the large-scale structure that we observe at $33D$ is the secondary vortex street which, under the absence of vortex shedding, appears around $25D$ downstream of bluff bodies (Cimbala *et al.* 1988; Huang & Keffer 1996). The above results suggest that the postulation of Bevilaqua & Lykoudis (1978) is indeed correct, i.e. that self-preservation is a result of the formation of large vortices, capable of linking the mean flow with the 'main turbulent motion'.

### 3.2.2. *Intermittency*

We now turn our attention to the intermittency of the flow by distinguishing between large-scale-dominated external intermittency and small-scale, internal, intermittency. Bevilaqua & Lykoudis (1978) showed that the presence of vortex shedding vortices increases large-scale intermittency near the edges of the wake, as their coherent motion induces alternations between slow fluctuations of low intensity (i.e. outer flow) and rapid fluctuations of high intensity (inner wake). This is something that we also observe in our measurements. Figure 11($a$) plots the intermittency coefficient $\Gamma$ at $40D$ for all plates; $\Gamma$ is defined as the inverse of the flatness of $\mathrm{d}u_x/\mathrm{d}x$ normalised by its minimum value over the radial profile at $x$ which is at, or very close to, $r = 0$. Therefore, $\Gamma$ is defined using the flatness of the velocity derivative, and not via its increments for a given scale separation. Moreover, it is normalised in a way that its value is one for a fully turbulent flow and drops to zero outside the wake's interface. In consequence, in the way we have defined it, and similarly to the approach taken in previous works (Townsend 1949), $\Gamma$ ultimately quantifies the radial dependency of the intermittency of the turbulent wake. The value of $\Gamma$ is much more sensitive to high values of $\mathrm{d}u_x/\mathrm{d}x$ than $C_1$, and so in the presence



https://doi.org/10.1017/jfm.2024.1197 Published online by Cambridge University Press

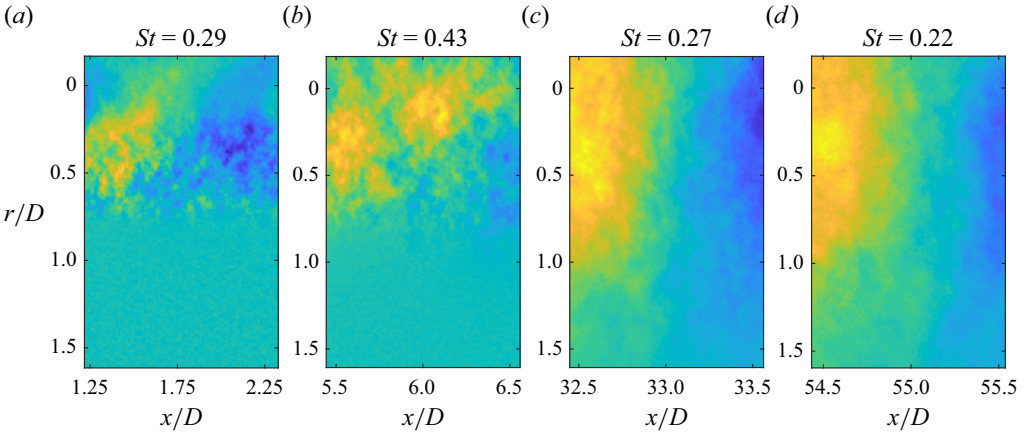


Figure 10. Shape of the first SPOD mode of the peak frequency of each curve of figure 9 for the PF plate. Note that the near wake ($x/D < 7$) exhibits shear layers instabilities, and the far wake $x/D > 30$ a well-defined vortex street, similar to the sketch of Huang & Keffer (1996) for two-dimensional porous plates, shown in figure 9(*b*).

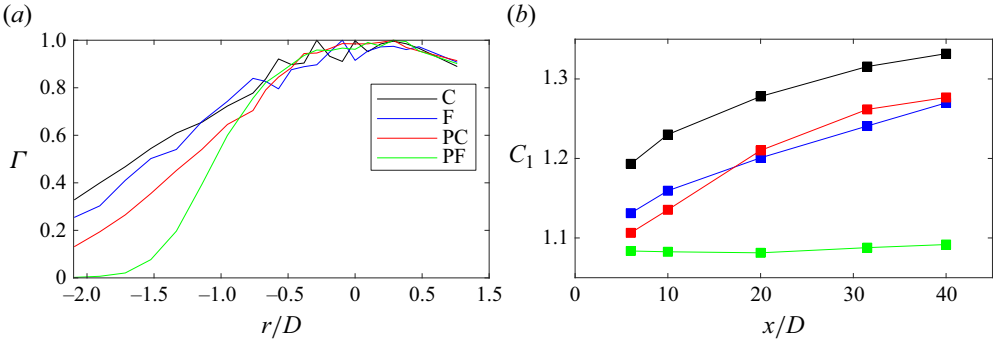


Figure 11. (*a*) Intermittency factor $\Gamma$ at $40D$ downstream of the plates and (*b*) $C_1$ coefficient at the centreline of the wake, for the four different plates. Both quantities were measured using HWA.

of a sharp dynamic interface between the inner turbulent wake and the outer laminar flow, slowly decreasing values of $\Gamma$ with increasing distance from the centreline reflect high large-scale-dominated external intermittency whereas a steep slope of $\Gamma$ suggests reduced large-scale-dominated external intermittency at the wake boundary (Townsend 1976; Bevilaqua & Lykoudis 1978). It can be observed that the slope of $\Gamma$ is steeper for the plates with lower vortex shedding intensity (e.g. the PF plate), as shedding promotes mixing: wakes with suppressed vortex shedding are thus expected to exhibit a sharper, and more 'insulated' boundary between the wake and the outer flow.

The above result is in agreement with the conclusions of Bevilaqua & Lykoudis (1978) regarding the large-scale 'interface' intermittency, where it was found that a wake with the absence of shedding exhibits steeper $\Gamma$ profiles compared with a wake dominated by vortex shedding (see figure 3 in Bevilaqua & Lykoudis 1978). Figure 11(*b*), however, shows a result concerning another type of intermittency, small-scale internal intermittency on the centreline where $\Gamma = 1$ and the flow is not in the proximity of the wake boundary but rather in the turbulent core. The coefficient $C_1$ at the centreline of the wake characterises the intermittency of the small scales of turbulence (see § 2.2.3) and it is plotted in



https://doi.org/10.1017/jfm.2024.1197 Published online by Cambridge University Press

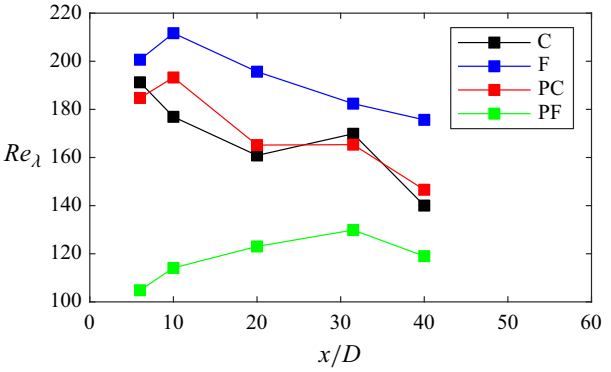


Figure 12. Reynolds number based on the Taylor microscale at the centreline of each plate measured via HWA.

figure 11(*b*) for all plates. The plates which exhibit vortex shedding show a consistent increase of small-scale intermittency with streamwise distance, while the PF plate exhibits small values very close to unity at all streamwise distances and therefore, effectively, near absence of small-scale intermittency (note that $C_1 = 1$ denotes absence of small-scale intermittency). Evidently, the shed vortices of the C, F and PC plates are more capable of affecting the small eddies of the flow, compared with the secondary street vortices of the PF plate. It is a highly non-trivial conclusion that the large-scale vortices can have such a big influence on the small-scale intermittency of the turbulence in the core of the wake. One may think that the absence of vortex shedding reduces the Reynolds number of the turbulence and thereby reduces small-scale intermittency as it is well known that small-scale turbulence is increasingly intermittent with increasing Reynolds number. Indeed, the Taylor length-based Reynolds number $Re_\lambda = \sqrt{\overline{u_x^2}}\lambda/\nu$ of the small-scale core turbulence measured via HWA is significantly larger for the C, F and PC plates than for the PF plate ($\lambda = \sqrt{15\nu\sqrt{\overline{u_x^2}}/\epsilon}$). This is shown in figure 12, where it can also be observed, however, that $Re_\lambda$ increases slightly with streamwise distance in the PF case whereas it decreases quite sharply in the C, F and PF cases for which $C_1$ in fact increases with streamwise distance. Low/high values of $C_1$ can therefore not be attributed to high/low values of $Re_\lambda$ in our flows. The evidence therefore suggests that small-scale intermittency in the core turbulence at the centre of the wake requires vortex shedding vortices. In fact, $Re_\lambda$ and $C_1$ are low in the PF case even in locations where the secondary street is shown to be prominent ($x/D > 30$), suggesting that it may not be just the presence of a large-scale coherent structure that matters for the appearance of small-scale intermittency at the core, but even the type of it.

### 3.2.3. *Wake recovery*

Finally, we investigate the effect of vortex shedding (or the absence of it) on the wake development. We consider a simplification of the Reynolds stress evolution equations, in which the pressure terms (pressure-rate-of-strain tensor) are considered to cause a redistribution of energy among the Reynolds stresses (Pope 2000). The turbulent transport terms are assumed to attenuate the intense Reynolds stresses located at the shear layers of the flow (Pope 2000), decreasing in that way the turbulent production. We may thus assume



https://doi.org/10.1017/jfm.2024.1197 Published online by Cambridge University Press

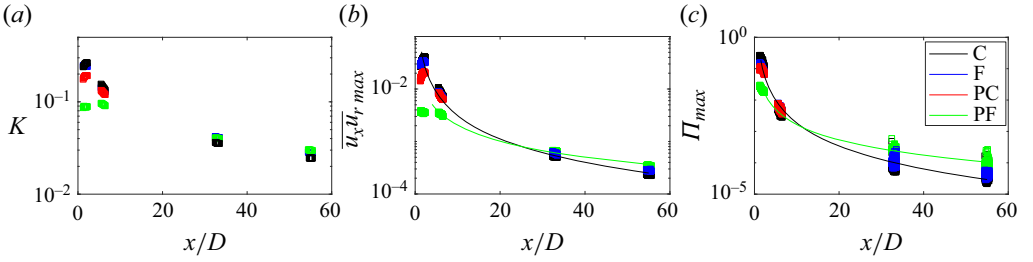


Figure 13. Maximum values over the radial direction of (*a*) turbulence kinetic energy, (*b*) Reynolds shear stress and (*c*) production of the streamwise Reynolds stresses, as functions of the downstream distance, at the four PIV windows. The plates are as shown in (*c*). The solid lines are power-law fits.

that, in our simplifying consideration, the effect of turbulent transport can be grouped with that of the dissipation term $\epsilon$. We thus end up with turbulence stresses which are attenuated by dissipation $\epsilon$, redistributed within its various components by the fluctuating pressure and augmented by the production terms (themselves a product of turbulent fluctuations with the velocity gradient $\partial U_x/\partial r$). We note that the dissipation term of the Reynolds shear stress can be either positive or negative, but its value is expected to be negligible away from solid boundaries (Pope 2000). We also note that the production term of the radial Reynolds stress component, $\overline{u_r^2}$, is negligible in the far wake.

The above simplified representation may be used to shed some light on the flow evolution. The starting point can be thought to be the 'bluffness' of the tested body. If it is bluff enough, it will cause a mean recirculation in its wake: wakes like that exhibit large negative convective velocities, and can be thus thought to be prone to absolute instabilities, i.e. vortex shedding (see discussion in § 2.2.2). Indeed, among the plates tested, C, F and PC exhibit an (absolute) vortex shedding instability (see § 3.1.1) and recirculation (see figure 15*a*). On the other hand, the PF plate lacks a recirculation region, and thus any perturbations are convected downstream by the average flow, rather than staying put. In that case, the instabilities are convective in nature (see § 2.2.2).

If vortex shedding emerges (absolute instability), it will cause an increase of turbulent fluctuations by an order of magnitude (see for instance figure 5), amplifying in that way the production of Reynolds stresses in the near wake (as production of Reynolds stresses is proportional to the magnitude of these stresses). Reynolds stresses will thus increase, and by extension, their dissipation. This intuitive result is verified using our PIV and HWA data in figures 13 and 14(*a*), where, at the near wake, the plates with the larger vortex shedding intensities (e.g. C and F), exhibit larger maximum turbulence kinetic energies $K$, Reynolds shear stresses and production/dissipation terms of the streamwise velocity variance. Using our PIV data, the turbulence kinetic energy is estimated as $K = 0.5(\overline{u_x^2} + \overline{u_r^2})/U_\infty^2$ (it was checked that a different estimation $K = 0.5(\overline{u_x^2} + 2\overline{u_r^2})/U_\infty^2$ does not alter the trends) and the production term of the streamwise Reynolds stresses, $u_x^2$, as $\Pi = 2\overline{u_x u_r}\partial U_x/\partial r + 2\overline{u_x^2}\partial U_x/\partial x$. The dissipation rate is calculated from the HWA data as $\epsilon = 15\nu \int k_w^2 E_{11}\, \mathrm{d}k_w$. $E_{11}$ is the one-dimensional energy spectrum and $\nu$ the kinematic viscosity.

Intense vortex shedding in the near wake will therefore generate high Reynolds shear stresses (as also seen in figure 5). In turn, the Reynolds shear stresses will generate strong streamwise velocity gradients $\partial U_x/\partial x$ through the average momentum equation (i.e. through the mixing of the wake with the outer flow). Considering a slowly expanding



https://doi.org/10.1017/jfm.2024.1197 Published online by Cambridge University Press

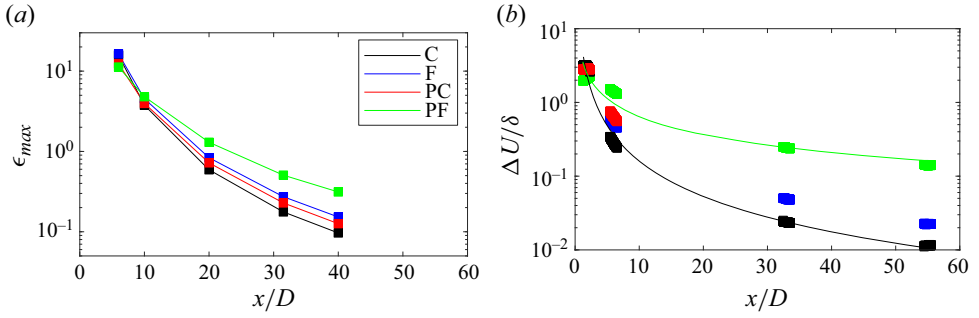


Figure 14. (*a*) Maximum dissipation rate of the HWA profiles measured for each plate, at four downstream distances and (*b*) $(U_{max} - U_{min})/\delta$ over downstream distance at the four PIV windows tested. The solid lines are power-law fits.

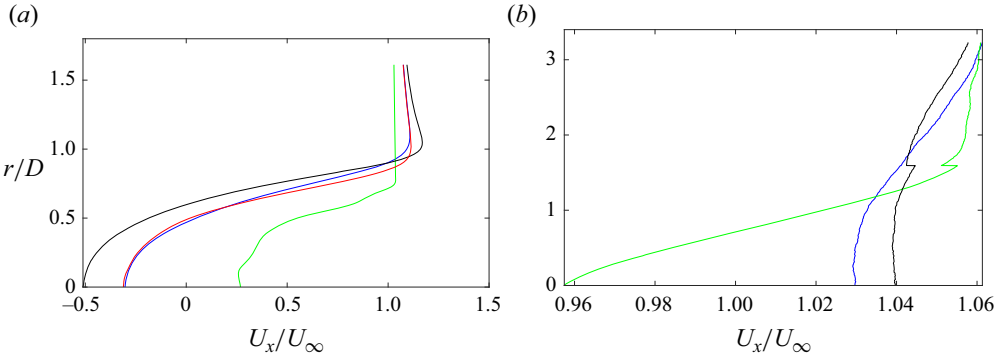


Figure 15. Average streamwise velocity distribution at (*a*) $x/D = 1.5$ and (*b*) $x/D = 55$. The colours are as in figure 14. The PF plate (green line) has the largest velocity deficit in the far wake, even though it initially exhibits the smallest deficit. Note the spike in the green curve in figure 15, due to the stitching of the two PIV windows.

wake (i.e. $\partial\delta/\partial x \approx 0$), and approximating $\partial U_x/\partial r \approx (U_\infty - U_x)/\delta$, we obtain

$$\frac{1}{\delta}\partial U_x/\partial x = -\frac{1}{\delta}\partial(U_\infty - U_x)/\partial x \approx -\frac{\partial}{\partial x}(\partial U_x/\partial r). \tag{3.2}$$

A strong gradient $\partial U_x/\partial x$ will thus lead to a strongly negative $\partial/\partial x(\partial U_x/\partial r)$, i.e. a fast wake recovery for the plates with intense vortex shedding. This is verified in figure 14(*b*), where the wakes with larger shedding end up having the smallest velocity deficit in the far wake (largest recovery), despite starting from larger velocity deficits in the near wake. The velocity deficit difference is illustrated in figure 15, which compares the normalised streamwise velocity distribution at $x/D = 1.5$ (near wake) and $x/D = 55$ (far wake) for the C, F and PF plates.

Finally, the fast wake recovery of the plates with vortex shedding, will lead to the abrupt attenuation of the production term (as the production term scales with the mean velocity gradient). This is verified in figure 13(*c*), where the plates with higher vortex shedding (and quicker wake recovery) exhibit a faster decay of their production term, compared with the plates with weaker shedding. Given that high-shedding plates also exhibit higher initial dissipation rates, the above result suggests a faster decay of turbulence for the high-shedding plates in the far wake. This is validated in figure 13(*a*,*b*), for the C and F plates, when compared with the PF plate.



https://doi.org/10.1017/jfm.2024.1197 Published online by Cambridge University Press

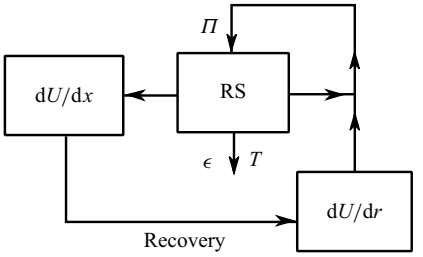


Figure 16. Simplified loop diagram of the recovery of a turbulent wake. Here, $\Pi$, $\epsilon$, $T$ and $RS$ stand for Reynolds stress production, dissipation, turbulent transport and Reynolds stresses, respectively. Pressure is assumed to only contribute to Reynolds stress redistribution. Vortex shedding gives an initial amplification of the Reynolds stresses, speeding up the recovery process.

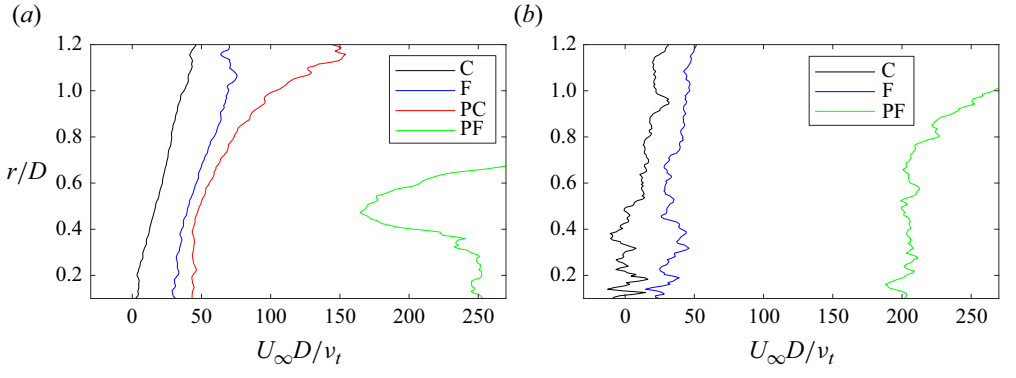


Figure 17. Normalised eddy viscosity profiles at (*a*) $x/D \approx 6$ and (*b*) $x/D \approx 33$.

The above simplified process is summarised in figure 16, which illustrates the process of wake recovery: high vortex shedding (initial, large Reynolds stresses) will accelerate the steps which lead to recovery. The PF plate wake that lacks vortex shedding and only develops large coherent structures in the far wake (i.e. secondary vortex street) exhibits the slowest evolution, retaining the largest momentum deficit and turbulence properties (i.e. Reynolds stresses, dissipation) of the four tested plates in the far wake, despite its initial condition being the mildest. A variation of intensity in vortex shedding thus has a significant effect on the wake's turbulence properties and on their relation with the mean flow. This can be further seen by plotting the distribution of the normalised eddy viscosity (see figure 17), calculated as $\nu_t = -\overline{u_x u_r}/(\partial U_x/\partial r)$ for the different plates. It can be seen that an increase in shedding intensity leads to an increase in the eddy viscosity of the flow.

## 4. Summary and conclusions

This work presents an experimental study of the influence of vortex shedding intensity on the near and far wake of bluff bodies. Four plates were tested using high-speed planar PIV and HWA, and their flow fields were analysed using a combination of SPOD, linear stability analysis of the mean flow and inspection of their turbulence statistics. Variation of the vortex shedding intensity, and its elimination, was achieved by modifying standard flat plates via the separate/combined effects of porosity, and multiscale perimeter.

Vortex shedding is found to be intimately connected to the mean-flow field. In particular, the vortex shedding Strouhal number of our tested plates, when the mean velocity



https://doi.org/10.1017/jfm.2024.1197 Published online by Cambridge University Press

gradient was used in the normalisation, exhibited the value that was postulated by Roshko (1955) to be universal for vortex shedding. This implies a strong connection between mean flow and turbulent fluctuations induced by the presence of coherent structures. According to the hypothesis of Bevilaqua & Lykoudis (1978), this connection is also responsible for the emergence of self-preservation in turbulent wakes, contrary to the hypothesis of Townsend (1956, 1970, 1976) that self-preservation is the effect of a loss of memory of initial conditions. Our results are in favour of the arguments in Bevilaqua & Lykoudis (1978), as we have found that the onset of self-preservation is accelerated when vortex shedding vortices (which carry the memory of initial conditions) are present. Our results also suggest that if vortex shedding is suppressed, self-preservation appears when other large-scale structures (in our case, the secondary vortex street) have had time to form, giving further credibility to the hypothesis of Bevilaqua & Lykoudis (1978). The presence/absence of vortex shedding enhances/depletes the large-scale intermittency at the edges of the wake, but also the small-scale intermittency at the centreline of the wake. The latter result is particularly compelling, as it implies that the degree of small-scale intermittency is directly controlled by large-scale structures. Finally, we have studied the evolution of the wake statistics by using theoretical arguments and our experimental results and have found that the presence of strong shed vortices accelerates the growth of Reynolds stresses and the recovery of the wake, bringing it to a well-mixed state sooner than otherwise. By contrast, the wake of the porous–fractal plate, which is the one that lacks vortex shedding, retains relatively high values of velocity deficits and Reynolds stresses for long streamwise distances, even if its initial condition is that of a relatively mild/weak wake. Future work should focus on uncovering the physical mechanisms that link large-scale coherent structures, self-preservation and small-scale intermittency.

**Acknowledgements.** The experiments were conducted during the 2021 and 2022 Lille Turbulence Programmes. K.S. is grateful to V. Gupta for providing access to the stability analysis code and to Y. Hwang for useful discussions. J.C.V. acknowledges funding by the European Union (ERC Advanced Grant NoStaHo, project number 101054117). Views and opinions expressed are, however, those of the author(s) only and do not necessarily reflect those of the European Union or the European Research Council. Neither the European Union nor the granting authority can be held responsible for them.

**Declaration of interests.** The authors report no conflict of interest.

**Author ORCIDs.**
K. Steiros https://orcid.org/0000-0001-7779-170X;
M. Obligado https://orcid.org/0000-0003-3834-3941;
C. Cuvier https://orcid.org/0000-0001-6108-6942;
J.C. Vassilicos https://orcid.org/0000-0003-1828-6628.

## Appendix A. Axial symmetry in the near wake of fractal plates

We test the axisymmetry of the near wake of the F and PF plates by conducting planar PIV measurements in two planes with a relative angle of 45°, as shown in figure 18(*a*) (note that F45 and PF45 refer to measurements conducted at the 45° angle plane for the F and PF plates, respectively). We first investigate the sensitivity of the coherent structures to the angle of measurement. Figure 18(*b*) shows that the eigenvalues of the first SPOD mode of the radial velocity are very similar for the different angles. A slight difference can be observed in the PF45 case, which exhibits the highest peak at $St = 0.49$, instead of the $St = 0.29$ of the PF case (however, we note that the differences in the magnitude of the eigenvalues are very small between the PF and PF45 cases). Figure 19 shows the eigenmode shapes corresponding to the highest eigenvalues of figure 18(*b*). The F45



https://doi.org/10.1017/jfm.2024.1197 Published online by Cambridge University Press

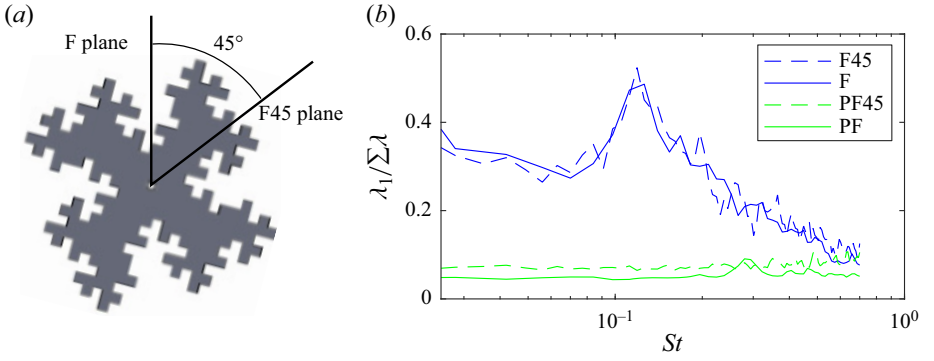


Figure 18. (*a*) The two planes for which PIV was acquired, with 45° between them. (*b*) Eigenvalue of the first SPOD mode for the radial velocity component, normalised with the sum of the eigenvalues for all modes, evaluated at each *St* for the F and PF plates, at two angles.

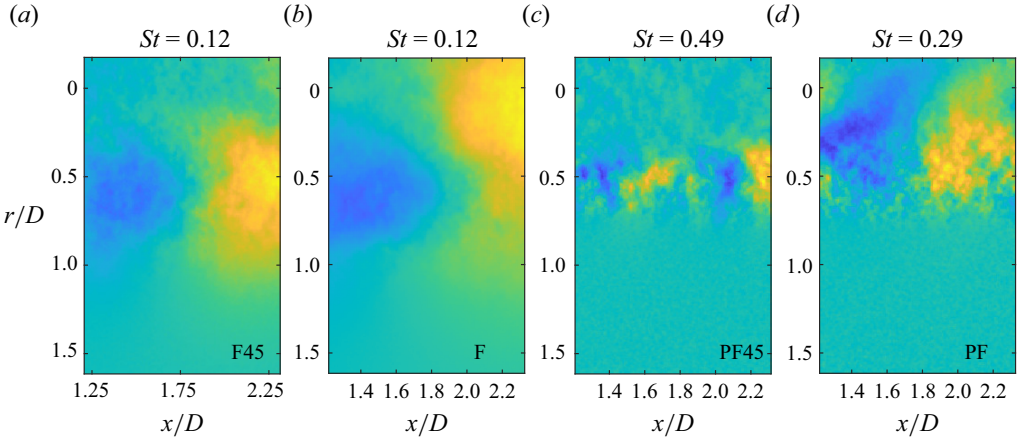


Figure 19. Shape of the first SPOD mode of the peak frequency of each curve of figure 18(*b*) for the F and PF plates.

case suggests an outward displacement of the vortex structure, compared with the one corresponding in the F case – this is likely because the F45 plane is behind an 'extrusion' of the fractal plate (see figure 18*a*). The most dominant mode of the PF plate exhibits larger shear-layer structures, compared with the PF45 case, as its corresponding Strouhal number is much lower.

Figures 20 and 21 compare the mean streamwise velocities and Reynolds shear stresses of the fractal plates. While there is very little variation in the mean velocity between the two angles of measurement, some differences can be observed in the Reynolds stresses: the F45 and PF45 plates exhibit more extensive shear layers compared with their zero-angle counterparts, as they are behind the 'extrusion' of the fractal. However, their maximum values remain approximately the same.

## Appendix B. Comparison of self-similar profiles for the various plates

In figure 22 we plot the curves of figure 8, but for each of the plates at the location 55*D* downstream, where all profiles are self-similar. To enable a better comparison between plates, we removed the stitching error of the PIV windows, by performing a 'crude'



https://doi.org/10.1017/jfm.2024.1197 Published online by Cambridge University Press

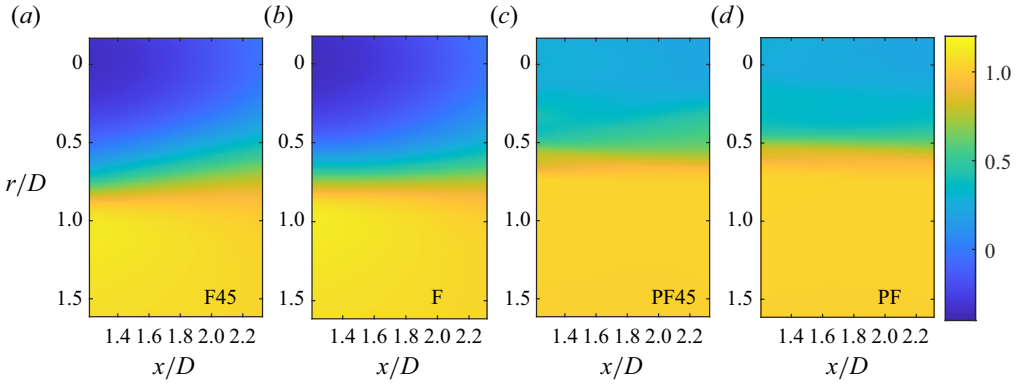


Figure 20. Normalised mean streamwise velocity ($U_x/U_\infty$) for the F and PF plates at two angles of measurement (see figure 18*a* for the plane angle).

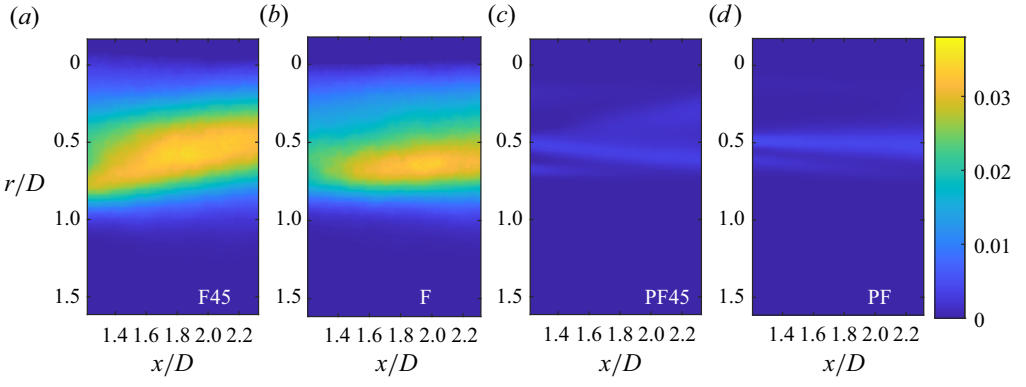


Figure 21. Normalised Reynolds shear stresses ($\overline{u_x u_r}/U_\infty^2$) for the F and PF plates at two angles of measurement (see figure 18*a* for the plane angle).

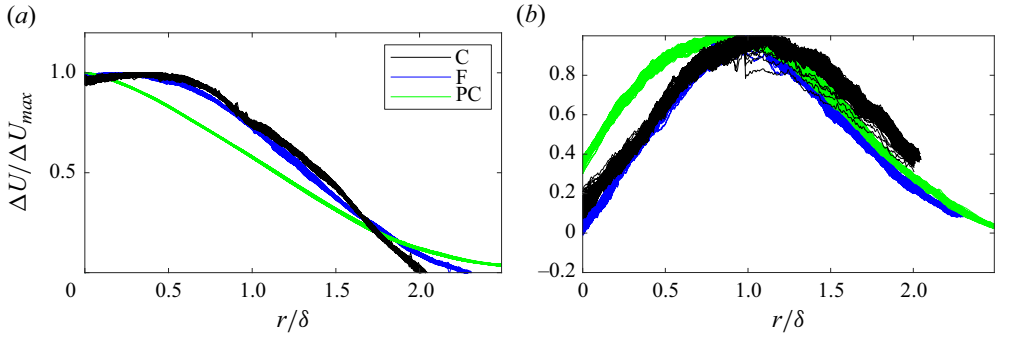


Figure 22. (*a*) Normalised velocity deficit and (*b*) normalised Reynolds shear stresses for various plates, 55*D* downstream.

correction where an identical shift of the statistics of the PIV2 window (see figure 1). We observe that, while the *C* and *F* plates have similar profiles (even though some differences persist), there is an evidently different distribution of both mean velocities and Reynolds shear stresses of the PF plate, compared with the plates with vortex shedding.



https://doi.org/10.1017/jfm.2024.1197 Published online by Cambridge University Press

## References


Alves Portela, F., Papadakis, G. & Vassilicos, J.C. 2018 Turbulence dissipation and the role of coherent structures in the near wake of a square prism. *Phys. Rev. Fluids* **3** (12), 124609.

Anderson, E.A. & Szewczyk, A.A. 1997 Effects of a splitter plate on the near wake of a circular cylinder in 2 and 3-dimensional flow configurations. *Exp. Fluids* **23** (2), 161–174.

Bempedelis, N. & Steiros, K. 2022 Analytical all-induction state model for wind turbine wakes. *Phys. Rev. Fluids* **7** (3), 034605.

Bevilaqua, P.M. & Lykoudis, P.S. 1978 Turbulence memory in self-preserving wakes. *J. Fluid Mech.* **89** (3), 589–606.

Cafiero, G. & Vassilicos, J.C. 2019 Non-equilibrium turbulence scalings and self-similarity in turbulent planar jets. *Proc. Math. Phys. Engng Sci.* **475** (2225), 20190038.

Castro, I.P. 1971 Wake characteristics of two-dimensional perforated plates normal to an air-stream. *J. Fluid Mech.* **46** (3), 599–609.

Castro, I.P. 2005 The stability of laminar symmetric separated wakes. *J. Fluid Mech.* **532**, 389–411.

Chongsiripinyo, K. & Sarkar, S. 2020 Decay of turbulent wakes behind a disk in homogeneous and stratified fluids. *J. Fluid Mech.* **885**, A31.

Cicolin, M.M., Chellini, S., Usherwood, B., Ganapathisubramani, B. & Castro, I.P. 2024 Vortex shedding behind porous flat plates normal to the flow. *J. Fluid Mech.* **985**, A40.

Cimbala, J.M., Nagib, H.M. & Roshko, A. 1988 Large structure in the far wakes of two-dimensional bluff bodies. *J. Fluid Mech.* **190**, 265–298.

Dairay, T., Obligado, M. & Vassilicos, J.C. 2015 Non-equilibrium scaling laws in axisymmetric turbulent wakes. *J. Fluid Mech.* **781**, 166–195.

Ferran, A., Aliseda, A. & Obligado, M. 2023 Characterising the energy cascade using the zero-crossings of the longitudinal velocity fluctuations. *Exp. Fluids* **64** (11), 176.

Gerrard, J.H. 1966 The mechanics of the formation region of vortices behind bluff bodies. *J. Fluid Mech.* **25** (2), 401–413.

Goto, S. & Vassilicos, J.C. 2016 Unsteady turbulence cascades. *Phys. Rev.* E **94** (5), 053108.

Grant, H.L. 1958 The large eddies of turbulent motion. *J. Fluid Mech.* **4** (2), 149–190.

Gupta, V., He, W., Wan, M., Chen, S. & Li, K.B.L. 2020 A Ginzburg–Landau model for linear global modes in open shear flows. *J. Fluid Mech.* **904**, A31.

Gupta, V. & Wan, M. 2019 Low-order modelling of wake meandering behind turbines. *J. Fluid Mech.* **877**, 534–560.

Huang, Z., Kawall, J.G. & Keffer, J.F. 1996 Development of structure within the turbulent wake of a porous body. Part 2. Evolution of the three-dimensional features. *J. Fluid Mech.* **329**, 117–136.

Huang, Z. & Keffer, J.F. 1996 Development of structure within the turbulent wake of a porous body. Part 1. The initial formation region. *J. Fluid Mech.* **329**, 103–115.

Hwang, Y. & Choi, H. 2006 Control of absolute instability by basic-flow modification in a parallel wake at low Reynolds number. *J. Fluid Mech.* **560**, 465–475.

Jiang, H. & Cheng, L. 2019 Transition to the secondary vortex street in the wake of a circular cylinder. *J. Fluid Mech.* **867**, 691–722.

Kirchhoff, G. 1869 Zur theorie freier flüssigkeitsstrahlen. *J. reine angezo. Math.* **70**, 289–298.

Kupfer, K., Bers, A. & Ram, A.K. 1987 The cusp map in the complex-frequency plane for absolute instabilities. *Phys. Fluids* **30** (10), 3075–3082.

Law, Y.Z. & Jaiman, R.K. 2018 Passive control of vortex-induced vibration by spanwise grooves. *J. Fluids Struct.* **83**, 1–26.

Liepmann, H.W. & Robinson, M.S. 1953 Counting methods and equipment for mean-value measurements in turbulence research. *NACA Tech. Rep.* 3037. NACA.

Lumley, J.L. 1970 *Stochastic Tools in Turbulence*. Courier Corporation.

Malkus, W.V.R. 1956 Outline of a theory of turbulent shear flow. *J. Fluid Mech.* **1** (5), 521–539.

Mantič-Lugo, V., Arratia, C. & Gallaire, F. 2014 Self-consistent mean flow description of the nonlinear saturation of the vortex shedding in the cylinder wake. *Phys. Rev. Lett.* **113** (8), 084501.

Mazellier, N. & Vassilicos, J.C. 2008 The turbulence dissipation constant is not universal because of its universal dependence on large-scale flow topology. *Phys. Fluids* **20**, 015101.

Mora, D.O., Pladellorens, E.M., Turró, P.R., Lagauzere, M. & Obligado, M. 2019 Energy cascades in active-grid-generated turbulent flows. *Phys. Rev. Fluids* **4** (10), 104601.

Nedić, J., Ganapathisubramani, B. & Vassilicos, J.C. 2013*a* Drag and near wake characteristics of flat plates normal to the flow with fractal edge geometries. *Fluid Dyn. Res.* **45** (6), 061406.

Nedić, J., Vassilicos, J.C. & Ganapathisubramani, B. 2013*b* Axisymmetric turbulent wakes with new nonequilibrium similarity scalings. *Phys. Rev. Lett.* **111** (14), 144503.




https://doi.org/10.1017/jfm.2024.1197 Published online by Cambridge University Press

OBLIGADO, M., DAIRAY, T. & VASSILICOS, J.C. 2016 Nonequilibrium scalings of turbulent wakes. *Phys. Rev. Fluids* **1** (4), 044409.
ORTIZ-TARIN, J.L., NIDHAN, S. & SARKAR, S. 2021 High-Reynolds-number wake of a slender body. *J. Fluid Mech.* **918**, A30.
POPE, S.B. 2000 *Turbulent Flows*. Cambridge University Press.
PRASAD, A. & WILLIAMSON, C.H.K. 1997 The instability of the shear layer separating from a bluff body. *J. Fluid Mech.* **333**, 375–402.
ROSHKO, A. 1955 On the wake and drag of bluff bodies. *J. Aeronaut. Sci.* **22** (2), 124–132.
SIEBER, M., PASCHEREIT, C.O. & OBERLEITHNER, K. 2016 Spectral proper orthogonal decomposition. *J. Fluid Mech.* **792**, 798–828.
STEIROS, K., BEMPEDELIS, N. & DING, L. 2021 Recirculation regions in wakes with base bleed. *Phys. Rev. Fluids* **6** (3), 034608.
STEIROS, K., BRUCE, P.J.K., BUXTON, O.R.H. & VASSILICOS, J.C. 2017 Effect of blade modifications on the torque and flow field of radial impellers in stirred tanks. *Phys. Rev. Fluids* **2** (9), 094802.
STEIROS, K. & HULTMARK, M. 2018 Drag on flat plates of arbitrary porosity. *J. Fluid Mech.* **853**, R3.
STEIROS, K., KOKMANIAN, K., BEMPEDELIS, N. & HULTMARK, M. 2020 The effect of porosity on the drag of cylinders. *J. Fluid Mech.* **901**, R2.
TENNEKES, H. & LUMLEY, J.L. 1972 *A First Course in Turbulence*. MIT Press.
TOWNE, A., SCHMIDT, O.T. & COLONIUS, T. 2018 Spectral proper orthogonal decomposition and its relationship to dynamic mode decomposition and resolvent analysis. *J. Fluid Mech.* **847**, 821–867.
TOWNSEND, A.A. 1949 The fully developed wake of a circular cylinder. *Austral. J. Chem.* **2** (4), 451–468.
TOWNSEND, A.A. 1970 Entrainment and the structure of turbulent flow. *J. Fluid Mech.* **41** (1), 13–46.
TOWNSEND, A.A.R. 1956 *The Structure of Turbulent Shear Flow*. Cambridge University Press.
TOWNSEND, A.A.R. 1976 *The Structure of Turbulent Shear Flow*, 2nd edn. Cambridge University Press.
TRIANTAFYLLOU, G.S., KUPFER, K. & BERS, A. 1987 Absolute instabilities and self-sustained oscillations in the wake of circular cylinders. *Phys. Rev. Lett.* **59** (17), 1914.
WILLIAMSON, C.H.K. 1996 Vortex dynamics in the cylinder wake. *Annu. Rev. Fluid Mech.* **28** (1), 477–539.
WILLIAMSON, C.H.K. & GOVARDHAN, R. 2004 Vortex-induced vibrations. *Annu. Rev. Fluid Mech.* **36**, 413–455.
WILLIAMSON, C.H.K. & PRASAD, A. 1993 A new mechanism for oblique wave resonance in the 'natural' far wake. *J. Fluid Mech.* **256**, 269–313.
WYGNANSKI, I., CHAMPAGNE, F. & MARASLI, B. 1986 On the large-scale structures in two-dimensional, small-deficit, turbulent wakes. *J. Fluid Mech.* **168**, 31–71.

https://doi.org/10.1017/jfm.2024.1197 Published online by Cambridge University Press